Observation of the shock-induced β-Sn to b.c.t.-Sn transition using time-resolved X-ray diffraction

R. Briggs,[a,b]* R. Torchio,[a] A. Sollier,[c] F. Occelli,[c] L. Videau,[c] N. Kretzschmar[a] and M. Wulff[a]

[a]European Synchrotron Radiation Facility, BP 220, F-38043 Grenoble Cedex, France, [b]Lawrence Livermore National Laboratory, 6000 East Avenue, Livermore, CA 94500, USA, and [c]CEA, DAM, DIF, F-91297 Arpajon, France. *Correspondence e-mail: briggs14@llnl.gov

Time-resolved X-ray diffraction measurements have been carried out on dynamically compressed Sn up to a maximum pressure of ∼13 GPa at the European Synchrotron Radiation Facility. The phase transition from β-Sn to body-centered tetragonal (b.c.t.) Sn has been observed using synchrotron X-ray diffraction for the first time undergoing shock compression and release. Following maximum compression, the sample releases to lower pressures for several nanoseconds until the reverse transition occurs. The data are in good agreement with previous shock boundaries that indicate that the β-Sn phase is stable ∼2 GPa higher than the static boundary upon compression and the b.c.t.-Sn phase is stable ∼1 GPa lower upon release. The transition to the high-pressure phase reveals a loss of texture in the X-ray diffraction data from the 'quasi' single-crystal β-Sn structure to a more powder-like Debye–Scherrer ring.

1. Introduction

Tin has been comprehensively studied at extreme conditions of high pressure and high temperature and its phase diagram has been explored using synchrotron X-ray diffraction techniques, in combination with diamond anvil cells to generate high pressures, to probe crystallographic structures over a wide range of P–T space. A transition from the ambient β-Sn structure to the body-centered tetragonal (b.c.t.) polymorph was first observed at 9.8 GPa (Barnett *et al.*, 1966). The phase boundary has a negative Clapeyron slope up to the β-Sn – b.c.t.-Sn – liquid triple point at 3.8 GPa and 580 K. Recent experiments investigated the room-temperature compression pathway up to much higher pressures, revealing transitions to body-centered orthorhombic (b.c.o.) at $P \simeq 32$ GPa, body-centered cubic (b.c.c.) at $P \simeq 40$ GPa and a hexagonally closed pack (h.c.p.) structure at $P \simeq 157$ GPa (Salamat *et al.*, 2013; 2011). Interestingly, both the b.c.o. and b.c.c. structures are observed between 40 and 70 GPa (Salamat *et al.*, 2013; Christensen & Methfessel, 1993). Calculations revealed that the b.c.c. polymorph would become re-entrant above 1300 GPa (1.3 TPa) as an electride structure (Salamat *et al.*, 2011; Pickard & Needs, 2010). The melting curve and high-temperature phase region have also been explored up to 105 GPa using synchrotron X-ray techniques (Briggs *et al.*, 2012; Briggs, Daisenberger *et al.*, 2017).

Whilst the determination of crystallographic phases at static high pressure using synchrotron X-ray diffraction is a well established field of research, the structural observation of each phase and their corresponding transition boundaries under rapid dynamic compression has been a significant challenge.
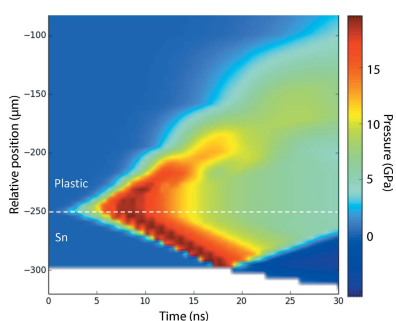
Historically, two-wave structure data have been indicative of phase transitions where the crystal structure determination has been through interpretation of diamond anvil cell measurements (Smith *et al.*, 2008). Sound speed measurements have been carried out in Sn, where a kink in the measured sound speeds has been used to suggest a phase transition in Sn along the principal shock Hugoniot (the loci of P–T points that can be accessed during shock compression) (Mabire & Héreil, 2014; Hu *et al.*, 2008). In the latter experiments (Hu *et al.*, 2008), the sound velocity measurements revealed a kink at $P \simeq 39$ GPa, which was interpreted as incipient melting along the Hugoniot. However, in both shock experiments, no *in situ* crystallographic information was measured to confirm the crystal structure of the high-pressure phases during compression.

Previously, dynamic ramp compression measurements have probed the crystal structure of Sn from ∼157 to 1197 GPa (1.2 TPa) (Lazicki *et al.*, 2015). In those experiments, the entropy gain of the sample was minimized to ensure the sample was probed in the solid region of the phase diagram. Diffraction was collected using image plate detectors to record the diffracted X-rays from the sample. Due to a large amount of background noise generated by the laser drive, only a single Bragg peak was observed above the background at the highest pressure, and a fit to the crystal structure was dependent on comparisons with the expected density obtained from velocimetry diagnostics. Interestingly, no h.c.p. phase was observed during the dynamic compression experiments and only the b.c.c. structure was observed. Now, owing to advances in third- and fourth-generation light sources, in particular X-ray free-electron lasers, phase transitions to complex crystal structures and liquid scattering can be observed directly (Briggs, Gorman *et al.*, 2017; Gorman *et al.*, 2015).

Phase transition pressures determined *via* dynamic shock compression techniques are often higher than the static high-pressure boundaries obtained from diamond anvil cells (Smith *et al.*, 2008). In Sn, the phase boundary was mapped from sound velocity measurements with transitions observed ∼2 GPa higher (on compression) and ∼1 GPa lower (on release) than the static high-pressure phase boundary (Mabire & Héreil, 2014; Hu *et al.*, 2008). Single-bunch synchrotron X-ray diffraction, with sufficient photon flux on the sample, provides an opportune study of the onset of phase transitions. A recent experiment at the European Synchrotron Radiation Facility (ESRF) demonstrated single-bunch synchrotron X-ray absorption measurements of shock compressed iron (Torchio *et al.*, 2016). An X-ray diffraction study was carried out on Bi at the Advanced Photon Source that followed the complex structures upon release from high pressure, with the data agreeing closely with the expected phase boundaries from static measurements (Hu *et al.*, 2013).

Here we present the observation of the β-Sn to b.c.t.-Sn phase transition following laser shock compression, using single-bunch X-ray diffraction experiments carried out on the time-resolved beamline ID09 at the ESRF. The data show the transition from quasi single-crystal β-Sn diffraction to a powder diffraction ring of the high-pressure b.c.t. phase. The

compression pathway allows us to study the phase boundary on release from high pressure and shows good agreement with velocity measurements that indicate a boundary that is ∼1 GPa lower than the static high-pressure phase boundary and that the equilibrium phase boundary lies close to the static high-pressure boundary. β-Sn is also observed on compression to beyond the static phase boundary and is consistent with a shock transition boundary almost 2 GPa higher than static. These represent the first laser shock compression experiments with *in situ* X-ray diffraction measurements at the ESRF.

2. Experimental methods

Laser shock compression experiments were carried out on the ID09 time-resolved X-ray diffraction beamline of the ESRF. Samples of 25 µm-thick Sn foil (Goodfellow, 99%) were attached to plastic confinement material (PMMA or polycarbonate plastic) with thin glue layers (Fig. 1). A nanosecond laser ($\lambda = 1064$ nm) with a Gaussian pulse duration of 5 ns at full width at half-maximum (FWHM) was used in confinement geometry with laser energies <185 mJ. The laser spot size was focused, at the interface between the plastic and Sn sample, to a diameter of ∼250 µm, generating laser intensities up to ∼80.0 GW cm^{-2} (assuming zero energy loss across the intensity profile of the laser spot area). However, significant spatial intensity fluctuations are expected across the laser profile. To estimate the actual laser intensity on sample, we ran hydrocode simulations and adjusted the laser intensity of the hydrocode to best match the experimental data for a laser energy of 185 mJ.

Hydrodynamic simulations were carried out using the Esther hydrocode to visualize the pressure profile inside the Sn sample and estimate the laser intensity on the sample (Colombier *et al.*, 2005; Bardy *et al.*, 2016). Laser absorption was set to zero inside the confining material with a Gaussian laser pulse with a foot width of 15 ns, such that the FWHM corresponded to 5 ns. A distance–time plot is shown in Fig. 2 for a simulation with intensity set to 40.0 GW cm^{-2}. A line out of the profile at the plastic–Sn interface is shown in Fig. 3 by the blue line with crosses.
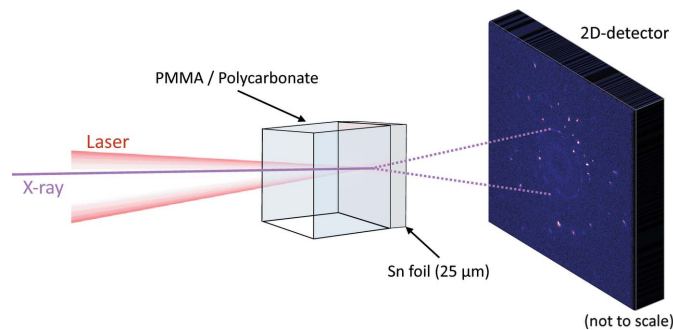

Figure 1
Sample and experimental geometry. The laser is focused to a diameter of ∼250 µm at the interface between plastic confinement and the Sn foil sample. The X-ray beam is aligned with the center of the laser spot and diffraction is recorded on the detector ∼80 mm from the sample.
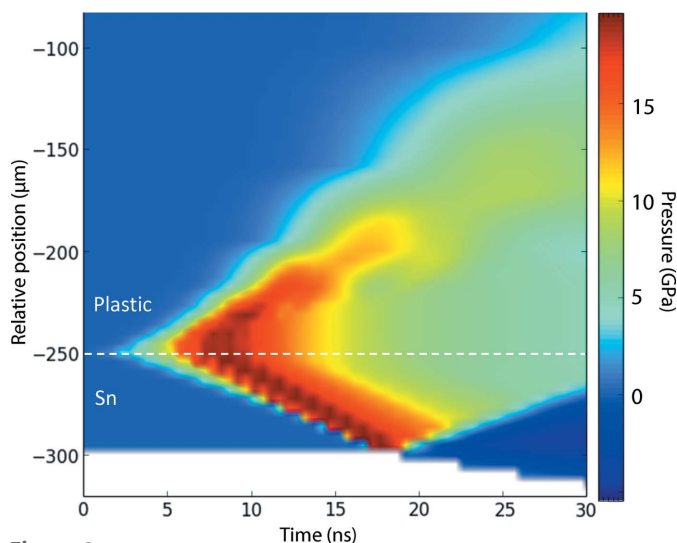
Figure 2
Position–time plot showing the pressure-loading history in the Sn sample (−250 to −290 µm) and plastic confinement region (−100 to −250 µm) for a laser intensity of 40 GW cm^{-2} using the Esther hydrocode. The dashed line indicates the loading interface between sample and plastic confinement and represents the pressure profile shown in Fig. 3 as a function of time. The laser is incident from the positive relative direction and focused to the plastic–Sn interface.
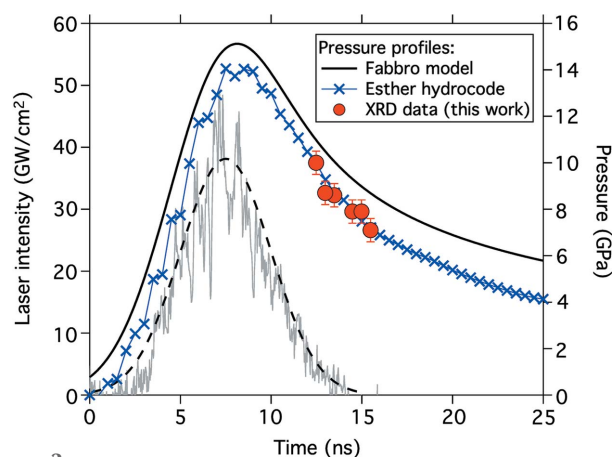

Figure 3
Intensity of the Gaussian laser pulse used in this experiment (gray profile) as a function of time. The dashed black line is a Gaussian profile scaled to the laser intensity with a FWHM of 5 ns. The solid black line is the time evolution of the pressure loading at the plastic–Sn interface from the Fabbro model; the blue line and crosses are the time evolution of the pressure loading from Esther hydrocode simulations shown in Fig. 2.

The confinement interaction model, developed by Fabbro and co-workers, is an analytical model that can be solved for simple laser temporal pulse profiles (square or triangular) or can also be solved numerically for any pulse profile (Fabbro *et al.*, 1990; Devaux *et al.*, 1993). In this study, we solve numerically the time evolution of the pressure and determine the maximum pressures for any given laser intensity. The model compares the shock impedance ($Z = \rho C_S$) of the confinement material (in this case PMMA plastic) and the sample (Sn) with a confinement corrective factor. The time evolution of the pressure profile in the Sn sample is shown in Fig. 3 along with the experimental Gaussian laser pulse profile

in gray. We see that the Fabbro model reaches a slightly higher pressure (within 1 GPa) than the Esther simulations that were used to match the experimental data. The pressure in the data is determined exclusively from the volume extracted from X-ray diffraction analysis and compared with the static high-pressure equation of state (Salamat *et al.*, 2013).

The X-ray spot size on the sample was ∼60 µm (V) × 100 µm (H). A U17 undulator was used to deliver ∼3.7 × 10^8 photons (10 mA)$^{-1}$ of the single-bunch current in the synchrotron pulse train. The X-ray energy was ∼15 keV, with a wavelength λ = 0.8265 Å. In order to perform a time-resolved study, the laser delay was synchronized to the ESRF radio frequency clock and could be adjusted in incremental steps of 0.5 ns. X-ray diffraction images were collected on a Rayonix MX170 HS detector in 2 × 2 binning mode. The corresponding pixel size was 88.6 µm × 88.6 µm. The sample-to-detector distances were calibrated and azimuthally integrated using *Dioptas* (Prescher & Prakapenka, 2015). Further details of the optical setup of the ID09b beamline can be found in the work of Wulff *et al.* (2003).

3. Results

X-ray diffraction measurements were collected at different laser energies with acquisitions at incremental time delays with respect to the laser initiation. X-ray diffraction images were also collected before each laser acquisition (with the sample at ambient conditions) to reveal the individual single-crystal reflections of the Sn foil (randomly oriented around the Debye–Scherrer ring). By adjusting the laser/X-ray delay, we were able to probe the sample at different pressure states of the pressure–time history (Fig. 3).

As a consequence of the rise time of the pressure profile, which increases over several nanoseconds, there is always a small region (∼5 µm) of sample ahead of the compression wave that is compressed to different pressures according to the rising edge pressure profile. In each X-ray diffraction image, we observe this rising edge as compression of the β-Sn Bragg spots to higher 2θ values as the unit cell is compressed. The known crystal structures of β-Sn ($I4_1/amd$) and b.c.t.-Sn ($I4/mmm$) were used to fit each diffraction peak that is observed in the XRD data. Using the corresponding lattice parameters for each phase we were able to estimate the pressure from the room-temperature equation of state for Sn (Salamat *et al.*, 2013). Thermal expansion due to the relatively small increases in temperature along the shock Hugoniot is negligible at the pressures investigated here. The XRD data show several individual Bragg peaks corresponding to β-Sn at high pressure; the lowest pressure observed was 1.8 (5) GPa and the maximum pressure was 8.9 (5) GPa (with several Bragg spots at pressures intermediate to the minimum and maximum pressures due to the rising edge).

Several of the β-Sn Bragg peaks on compression are found along the same azimuthal direction as the uncompressed β-Sn single Bragg spots, indicating compression along the same orientation (Fig. 4). It is well established that an elastic wave travels immediately behind the shock front, followed by a
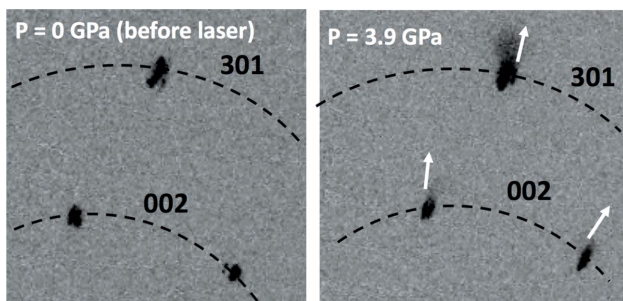
Figure 4
Close-up image of the 002 and 301 Bragg reflections of the β-Sn phase at ambient pressure (left) and during laser compression (right). The Bragg peaks are compressed along the same orientation (indicated by the white arrows) and index to the β-Sn phase at a pressure of 3.9 GPa.

plastic wave, after which any phase transformations can occur (Smith *et al.*, 2013). Recent experiments at the MEC end-station of the LCLS X-ray free-electron laser facility have used phase-contrast imaging during shock compression of silicon to identify the elastic/plastic regions behind the shock front (Nagler *et al.*, 2016). In these experiments, we have used X-ray diffraction and observed the compression of quasi single crystals along the same orientation, originating from the elastic compression wave. The additional Bragg peaks that appear are observed at new positions around the expected Debye–Sherrer ring for the β-Sn structure, but at slightly higher pressures. This indicates that plastic deformation has occurred as the higher-pressure crystallites have shifted in orientation under compression. These peaks are also slightly broader than the initial ambient peaks, indicating that the grain size has likely decreased. A similar observation was found in scandium under shock compression, which led to the broadening of the h.c.p. peaks upon compression (Briggs, Gorman *et al.*, 2017). Here we find there is no significant deformation during compression of β-Sn that would create a powder-like ring.

At the highest laser intensity (∼40 GW cm^{-2}) and between 12.5 and 15.5 ns, the formation of new diffraction peaks is observed. The new peaks are much more powder-like than the β-Sn single-crystal peaks, visible as an almost full Debye–Sherrer ring, and fit to the expected position of the high-pressure b.c.t.-Sn phase (Fig. 5); the integrated XRD patterns are shown in Fig. 6. The powder texture of b.c.t. Sn is consistent with a first-order phase transition from β-Sn as the large grains collapse and break due to a large volume decrease of ∼10%. However, we note that there is still some texture in the high-pressure phase as diffraction from several broad sections of the DS ring is observed, whilst part of the DS ring has zero intensity (Fig. 5).

The X-ray probe time was delayed in order to probe conditions upon release. As the delay time was increased, the pressure of the b.c.t.-Sn phase began to decrease as the drive intensity decreased. This is highlighted by the red dashed line in Fig. 6 that shows the peak position of the b.c.t.-Sn 101 peak shifting to smaller 2θ as the unit cell expands. The higher angle reflections are not observed due to the weak intensities and

the low number of counts on the detector. The lowest pressure observed for b.c.t.-Sn is 7.1 (5) GPa (blue profile in Fig. 6), which is ∼1 GPa lower than the static high-pressure boundary, showing excellent agreement with the b.c.t.-Sn/β-Sn boundary indicated from sound velocity measurements (Mabire & Héreil, 2014; Hu *et al.*, 2008).

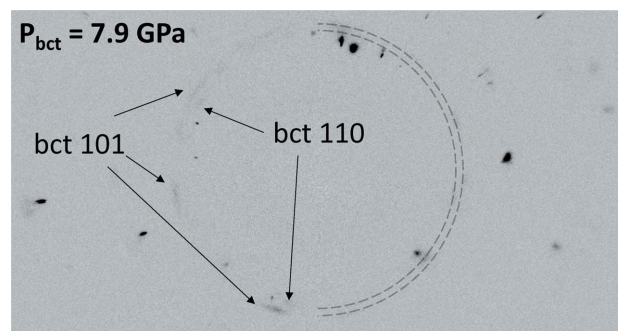Diffraction of the b.c.t.-Sn phase at maximum compression cannot be seen due to insufficient flux required to observe

Figure 5
Raw XRD image showing the faint powder-like diffraction ring that is formed by the high-pressure b.c.t.-Sn phase after compression. Dashed lines highlight the locations of the 101 and 110 b.c.t.-Sn peaks at 7.9 GPa (see Fig. 6 for the integrated XRD profile at *t* = 15 ns).
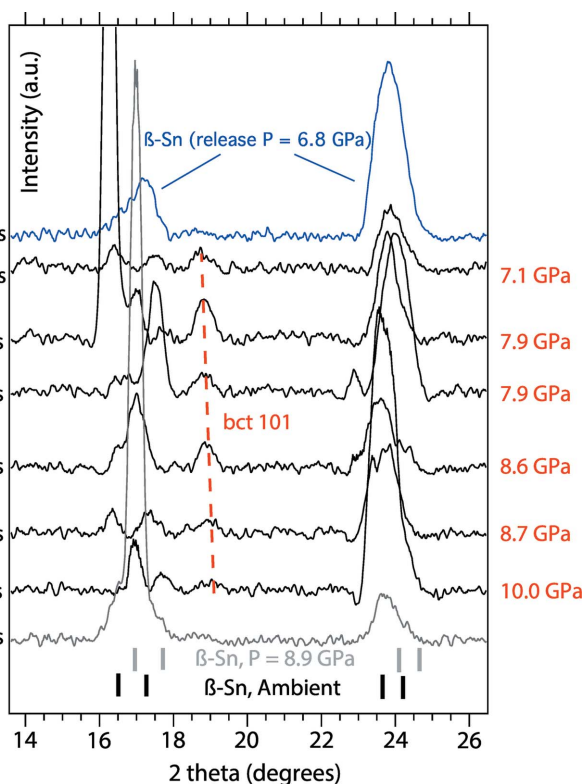

Figure 6
Integrated X-ray diffraction profiles collected at increasing time (from bottom to top) showing release of b.c.t.-Sn from the first observation at high pressure (10.0 GPa) to the lowest pressure observed (7.1 GPa). Each profile represents a separate data collection on a new area of the sample. After a period of time, the pressure in the compressed region of the sample was lower than 7.1 GPa and b.c.t.-Sn was not observed, which is in good agreement with the existing b.c.t.-Sn to β-Sn transition from shock studies.
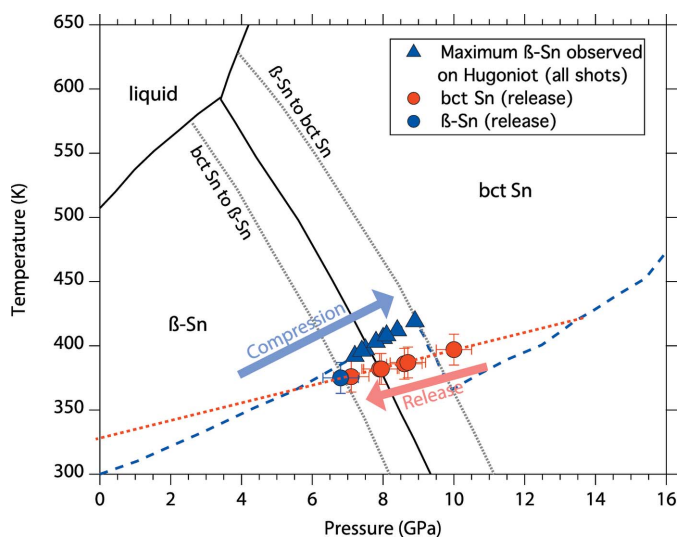
Figure 7
Phase diagram of Sn up to 16 GPa.

scattering from the small amount of material that is compressed at maximum pressure (P = 13.7 GPa from Fig. 3). At 12.0 ns we do not observe any diffraction from the b.c.t.-Sn phase, but do observe the β-Sn at a pressure of 8.1 (5) GPa. The maximum pressures for the β-Sn phase for each data collection from Fig. 6 are indicated by blue triangles in Fig. 7 and show excellent agreement with sound velocity measurements that show that the β-Sn/b.c.t.-Sn phase boundary is ~2 GPa higher than the static phase boundary. This over-pressurization of the phase boundary in Sn is perhaps not unsurprising considering there is a mixed-phase region between the β-Sn and b.c.t.-Sn phases of 9–16 GPa at room temperature during static compression experiments under hydrostatic conditions (Salamat *et al.*, 2013). However, it should be noted that the halfway point between the phase transition boundary on compression and release provides a dynamic equilibrium phase boundary that is much closer to the static phase boundary at $P \simeq 8.0$ (5) GPa near 400 K.

The results presented here using *in situ* crystallographic measurements support the β-Sn/b.c.t.-Sn phase boundaries at low pressure indicated by sound velocity measurements (Mabire & Héreil, 2014; Hu *et al.*, 2008). This therefore draws attention to further changes at higher pressures where there is a disagreement between previous shock data over the onset of incipient melting on the principal Hugoniot. In a more recent study, a significant jump in Eulerian sound velocity was observed at 34 GPa, attributed to the b.c.t.-Sn to b.c.c.-Sn phase transition, and was followed by a gradual transition to the bulk sound speed, starting at 39 GPa, which indicated the onset of melting and a solid–liquid coexistence range (Hu *et al.*, 2008). That study suggested that the earlier Hugoniot temperatures by Mabire and co-workers (Mabire & Héreil, 2014) were over-estimated as a consequence of glue layers affecting the measured radiance during shock compression at the interface between the Sn and window material. The onset of melting near 39 GPa would represent melting temperatures ~500 K lower than static DAC measurements that could not

be attributed to the same kinetic effects occurring during the β-Sn to b.c.t.-Sn transition.

4. Conclusions

In this paper we present the first X-ray diffraction measurements of the shock-induced β-Sn to b.c.t.-Sn phase transition (and reverse transition) using time-resolved X-ray diffraction. The high-pressure b.c.t.-Sn phase loses some of its texture during the transition from the ambient quasi single crystal to a powder diffraction ring as it undergoes a ~10% volume decrease. As the sample releases to lower pressure, we observed the b.c.t.-Sn phase until the reverse transition occurred at 7.0 GPa. β-Sn is observed up to 8.9 GPa and both the β-Sn/b.c.t.-Sn and reverse b.c.t.-Sn/β-Sn phase boundaries are in excellent agreement with those indicated by sound velocity measurements.

References

Bardy, S., Aubert, B., Berthe, L., Combis, P., Hébert, D., Lescoute, E., Rullier, J.-L. & Videau, L. (2016). *Opt. Eng.* **56**, 011014.
Barnett, J. D., Bean, V. E. & Hall, H. T. (1966). *J. Appl. Phys.* **37**, 875–877.
Briggs, R., Daisenberger, D., Lord, O. T., Salamat, A., Bailey, E., Walter, M. J. & McMillan, P. F. (2017). *Phys. Rev. B*, **95**, 054102–054108.
Briggs, R., Daisenberger, D., Salamat, A., Garbarino, G., Mezouar, M., Wilson, M. & McMillan, P. F. (2012). *J. Phys. Conf. Ser.* **377**, 012035.
Briggs, R., Gorman, M. G., Coleman, A. L., McWilliams, R. S., McBride, E. E., McGonegle, D., Wark, J. S., Peacock, L., Rothman, S., Macleod, S. G., Bolme, C. A., Gleason, A. E., Collins, G. W., Eggert, J. H., Fratanduono, D. E., Smith, R. F., Galtier, E., Granados, E., Lee, H. J., Nagler, B., Nam, I., Xing, Z. & McMahon, M. I. (2017). *Phys. Rev. Lett.* **118**, 025501.
Christensen, N. E. & Methfessel, M. (1993). *Phys. Rev. B*, **48**, 5797–5807.
Colombier, J. P., Combis, P., Bonneau, F., Le Harzic, R. & Audouard, E. (2005). *Phys. Rev. B*, **71**, 165406.
Devaux, D., Fabbro, R., Tollier, L. & Bartnicki, E. (1993). *J. Appl. Phys.* **74**, 2268–2273.

Fabbro, R., Fournier, J., Ballard, P., Devaux, D. & Virmont, J. (1990). *J. Appl. Phys.* **68**, 775–784.

Gorman, M. G., Briggs, R., McBride, E. E., Higginbotham, A., Arnold, B., Eggert, J. H., Fratanduono, D. E., Galtier, E., Lazicki, A. E., Lee, H. J., Liermann, H. P., Nagler, B., Rothkirch, A., Smith, R. F., Swift, D. C., Collins, G. W., Wark, J. S. & McMahon, M. I. (2015). *Phys. Rev. Lett.* **115**, 095701–095705.

Hu, J., Ichiyanagi, K., Doki, T., Goto, A., Eda, T., Norimatsu, K., Harada, S., Horiuchi, D., Kabasawa, Y., Hayashi, S., Uozumi, S.-I., Kawai, N., Nozawa, S., Sato, T., Adachi, S.-I. & Nakamura, K. G. (2013). *Appl. Phys. Lett.* **103**, 161904–161906.

Hu, J., Zhou, X., Dai, C., Tan, H. & Li, J. (2008). *J. Appl. Phys.* **104**, 083520–083527.

Lazicki, A., Rygg, J. R., Coppari, F., Smith, R., Fratanduono, D., Kraus, R. G., Collins, G. W., Briggs, R., Braun, D. G., Swift, D. C. & Eggert, J. H. (2015). *Phys. Rev. Lett.* **115**, 075502.

Mabire, C. & Héreil, P. L. (2014). *AIP Conf. Proc.* **505**, 93–96.

Nagler, B., Schropp, A., Galtier, E. C., Arnold, B., Brown, S. B., Fry, A., Gleason, A., Granados, E., Hashim, A., Hastings, J. B., Samberg, D., Seiboth, F., Tavella, F., Xing, Z., Lee, H. J. & Schroer, C. G. (2016). *Rev. Sci. Instrum.* **87**, 103701–103708.

Pickard, C. J. & Needs, R. J. (2010). *Nat. Mater.* **9**, 624–627.

Prescher, C. & Prakapenka, V. B. (2015). *High. Press. Res.* **35**, 223–230.

Salamat, A., Briggs, R., Bouvier, P., Petitgirard, S., Dewaele, A., Cutler, M. E., Corà, F., Daisenberger, D., Garbarino, G. & McMillan, P. F. (2013). *Phys. Rev. B*, **88**, 104104.

Salamat, A., Garbarino, G., Dewaele, A., Bouvier, P., Petitgirard, S., Pickard, C. J., McMillan, P. F. & Mezouar, M. (2011). *Phys. Rev. B*, **84**, 140104.

Smith, R. F., Bolme, C. A., Erskine, D. J., Celliers, P. M., Ali, S., Eggert, J. H., Brygoo, S. L., Hammel, B. D., Wang, J. & Collins, G. W. (2013). *J. Appl. Phys.* **114**, 133504.

Smith, R. F., Eggert, J. H., Saculla, M. D., Jankowski, A. F., Bastea, M., Hicks, D. G. & Collins, G. W. (2008). *Phys. Rev. Lett.* **101**, 065701.

Torchio, R., Occelli, F., Mathon, O., Sollier, A., Lescoute, E., Videau, L., Vinci, T., Benuzzi-Mounaix, A., Headspith, J., Helsby, W., Bland, S., Eakins, D., Chapman, D., Pascarelli, S. & Loubeyre, P. (2016). *Sci. Rep.* **6**, 26402.

Wulff, M., Plech, A., Eybert, L., Randler, R., Schotte, F. & Anfinrud, P. (2003). *Faraday Discuss.* **122**, 13–26.